Materials Transactions, Vol. 59, No. 5 (2018) pp. 835 to 842

Heat-Conduction-Type and Keyhole-Type Laser Welding of Ti–Ni Shape-Memory Alloys Processed by Spark-Plasma Sintering

Abdollah Bahador[1,*], Esah Hamzah[1,*], Katsuyoshi Kondoh[2], Seiichiro Tsutsumi[2], Junko Umeda[2], Tuty Asma Abu Bakar[1] and Farazila Yusof[3]

[1]*Faculty of Mechanical Engineering, Universiti Teknologi Malaysia, 81310 UTM Johor Bahru, Johor, Malaysia*
[2]*JWRI, Osaka University, Ibaraki 567-0047, Japan*
[3]*Department of Mechanical Engineering, Faculty of Engineering, University of Malaya, 50603 Kuala Lumpur, Malaysia*

High-brightness and high-power laser welding with different welding speeds and laser powers was applied to join Ti–51 at%Ni shape-memory alloy, which was fabricated from the elemental pure Ti and pure Ni powders by spark-plasma sintering. Dendritic microstructures were observed in all the welds except the heat-conduction-type weld with the minimum welding parameters. In addition, the weld seam consisted of equiaxial grains surrounded by a narrow dendritic region. Based on the micro-X-ray diffraction pattern, in the keyhole-type welding, the martensite phase declined on increasing laser power and welding speed. Abnormal peak intensities were detected for (211) in the heat-conduction weld and (200) in the keyhole weld. Differential scanning calorimetry results revealed that phase transformation peaks of the conduction-type weld seam were similar to the base metal of Ti–51 at%Ni SMA, whereas the corresponding peaks of the phase transformation in the other weld seams shifted towards lower temperatures due to Ni depletion in the matrix, grain coarsening and residual stress. Therefore, the findings suggest that heat-conduction-type can be a promising method for surface treatment of Ti–Ni SMAs with minimum effect on the microstructure and shape memory properties. [doi:10.2320/matertrans.M2017387]

(Received December 8, 2017; Accepted February 16, 2018; Published April 25, 2018)

Keywords: *shape-memory alloys, spark-plasma sintering, heat-conduction-type welding and keyhole-type welding*

1. Introduction

Ti–Ni shape memory alloys (SMAs) are widely used as biomedical implants even though recently β-Ti alloys are more attractive for researchers because of suspected negative effects of Ni.[1)] Joining of shape-memory alloys has been an interesting area for researchers because of its effect on the functional properties. Therefore, there has been a strong effort to find a suitable joining process to minimize the change in properties resulting from welding. Conventional fusion welding of Ti–Ni reduces the shape-memory properties due to severe metallurgical conversion in the heat-affected zone and fusion zone[2)] however, a recent report showed that there is an improvement in the joining of Ti–Ni SMAs by tungsten inert gas (TIG) welding.[3)] Laser welding is the most common joining process of Ti–Ni SMAs because of its high energy density and very low heat input, which leads to minimizing the welding distortion.[4)] Heat-conduction type and keyhole type are two main systems in the laser welding process. These welding modes are mainly distinguished by the power density they use; while the power density is inadequate to cause boiling in the conduction mode, the power density of the keyhole mode is high enough (depends on material) for boiling to take place in the weld pool. Despite different studies of these two welding modes, the boundaries between them are not clear in terms of processing parameters.[5)]

The effects of laser welding on the microstructure and mechanical properties of Ti–Ni SMAs has been reported in several research works.[6–9)] Laser welding of Ti–Ni SMAs results in different phase fractions of martensite and austenite. Oliveira *et al.*[10)] measured the phase fractions of Ti–50.8 at%Ni laser welds using a synchrotronic X-ray diffraction method. It was found that the martensite fraction decreased from the weld centreline towards the heat-affected zone due to privileged Ni volatilization in this region. The presence of martensite in the weld seam reduces superelastic properties of the welded joint. Because superelasticity properties are based on the B2 $\leftrightarrow$ B19′ reversible transformation, the full austenite phase is required to obtain higher amounts of recovered strains.

Despite casting processes of Ti–Ni SMAs, recently there has been an intention to use powder metallurgy to fabricate SMAs due to their advantages to prevent casting process problems such as segregation and grain growth.[11)] However, internal pores in the powder metallurgy components are one the main issues of this process, which affects the performance of the products. Spark-plasma sintering (SPS) is known as an advanced powder metallurgy technique whereby pores are reduced to a minimum, resembling cast materials. Successful utilization of SPS to synthesise Ti–Ni SMAs has been reported in recent years.[12,13)]

In the case of welding of powder metallurgy components, internal pore content needs to be considered to achieve a weld with high performance because pre-existing pores in the base metal contribute to the weld porosity formation and affect on the mechanical properties and performance.[14,15)]

In the previous research works, the most attention has been drawn on the welding of casting processed shape memory alloys and there are no systematically investigations to join powder processed shape memory alloys. Therefore, in the first step of this work, high density Ti–51 at%Ni SMAs was produced by SPS method and then bead on plate welding was applied with different welding parameters focused on comparing laser-welding regimes of heat-conduction-type and keyhole-type to understand weldability and phase transformation behaviour.

*Corresponding author, E-mail: esah@mail.fkm.utm.my, a79bahador@gmail.com

Table 1 Welding parameters used in this experiment.

Weld no and types	Welding speed (m/min)	Laser power (KW)	Heat input (KJ/mm)
C1	0.3	0.5	0.1
K1	3	1.5	0.03
K2	30	10	0.02
C2	0.3	1	0.2
K3	3	2	0.04
K4	30	12	0.04

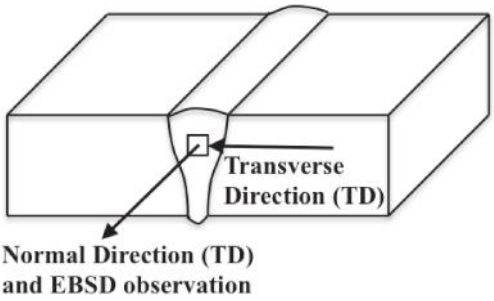

Fig. 1 Schematic drawing, direction of EBSD observation and inverse pole figure mapping.

2. Materials and Methods

In the current research, SPS (SPS-1030S, SPS Syntex system) was used to consolidate the mixed commercially pure Ti and Ni powders into a cylindrical billet of Ti–51 at%Ni SMAs with a diameter of 50 mm and 20 mm thickness. The relative density was calculated by Archimedes' principle and the results showed a high density of fabricated samples (nearly 99%). Specimens were cut by electrical-discharge machining (EDM) wire cut to get plate shape specimens. The homogenizing heat treatment process was carried out at 1000°C for 12 hours, with subsequent solution treatment at 1000°C for 1 hour. Finally, specimens underwent aging at 500°C for 1 hour and water quenched to introduce the desired lenticular Ti_3Ni_4 precipitates in order to improve shape-memory properties. Heat-conduction and keyhole-welding modes were utilized to determine the weldability and select the optimum conditions of the welding in terms of welding speed and laser power. Two keyhole-welding modes were used at medium and high values of welding parameters to produce four weld seams and two welds were produced by conduction. A continuous wave-disk laser (TRUMPF TruDisk 16002, wavelength: 1030 nm) with maximum laser power and the beam parameter product of 16 kW and 8 mm.mrad was used to create the welds. Focal length and spot size at focus point were 255 mm and 0.34 mm, respectively. To introduce an inert atmosphere, argon gas with a flow rate of 30 L/min was applied on the cap and root sides of the welds. Welding parameters (welding speed and laser power) are tabulated in Table 1 (C: conduction-type and K: keyhole-type welds). Heat input was calculated according to the following equation[16)]

$$Q = \frac{P}{S}, \tag{1}$$

where Q is heat input (kJ/mm), P is the laser output power (kW) and S is the welding speed (m/min).

A field emission scanning electron microscope (FESEM) (JEM-6500F, JEOL) coupled with an energy dispersive spectrometer (EDS) were used for line scan and elemental analysis. A micro-XRD system (Bruker-D8, CoKα1 radiation, wavelength 1.78897 Å) was used to investigate the phases present in the base metal and weld seam. Electron back-scatter diffraction (EBSD) (TSL EDAX DigiView IV) was used with a scanning step size of 0.5 μm to study the grain orientations. EBSD samples were electrochemically etched using acid solution with a volume ratio of CH_3COOH: $HClO_4 = 95:5$ at 20 V.[17)] As shown in Fig. 1, EBSD observation and inverse pole figure mappings were conducted in normal direction to the cross-section of the welds. EBSD test areas were selected from the centre of the fusion zones. Differential scanning calorimetry (DSC) (DSC-60 Shimadzu) under controlled cooling and heating rates of 10°C/min was used to determine the phase transformation temperatures of the welded seams and base metal. To make sure that carbon does not interfere during the powder metallurgy process and laser welding, carbon measurements were carried out using an infrared absorption carbon analyser system (HORIBA, EMIA-221V20K).

3. Results and Discussion

3.1 Weld seam features

The surface appearance of the weld seams is illustrated in Fig. 2. Based on visual inspection, the soundest weld belonged to C1 while C2 showed the worst appearance because of unacceptable weld seam width and discoloration owing to corrosion. K3 and K4, which were welded by high values of laser power and speed, displayed weld bead appearance including excess undercut and swellings, which are attributes of the humping regime in the melt pool.

Based on optical microscope analysis, a variety of weld seams were observed in terms of penetration, weld width and internal porosity. These factors directly affect the welds' quality and performance.[18)] Figure 3 shows that the morphology of the weld seams changed with welding parameters in both the heat-conduction-type and keyhole-type welds. The heat-conduction type with lower laser power displayed partial penetration and wide weld seams. Welding speed, as well as laser power, plays key roles in the weld width and penetration. According to eq. (1), by increasing the

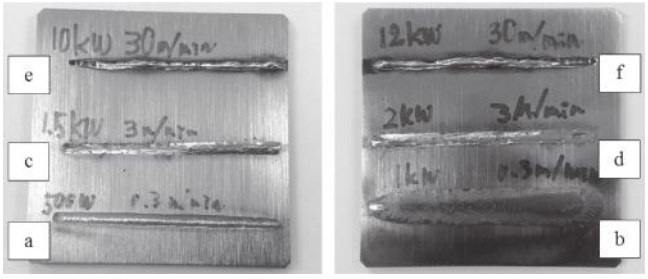

Fig. 2 Top view of the welds: (a) C1, (b) C2, (c) K1, (d) K2, (e) K3 and (f) K4.

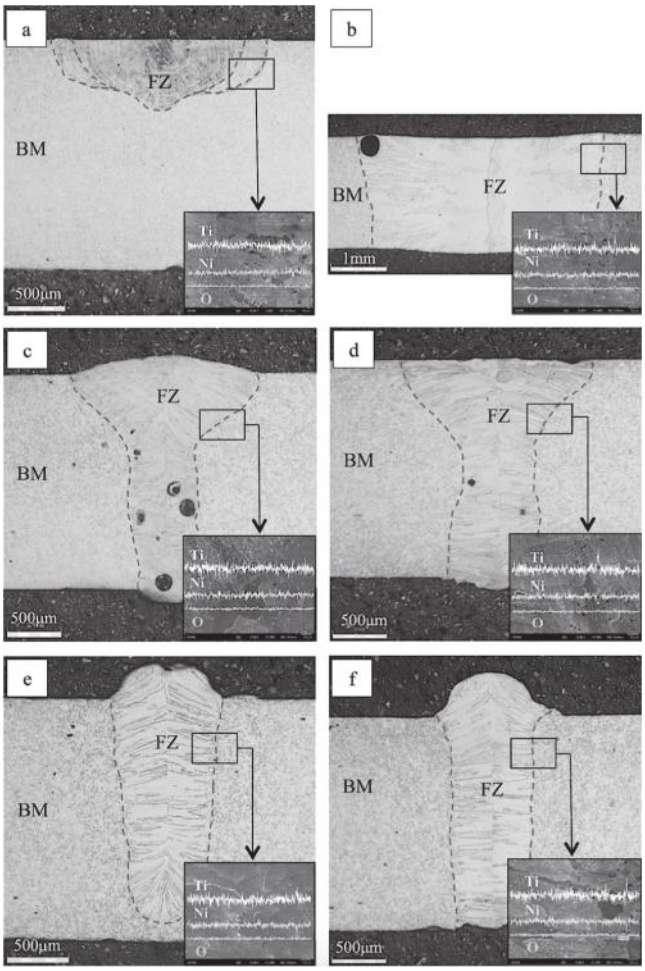

Fig. 3 The cross section and linear elemental analysis of the weld seams: (a) C1, (b) C2, (c) K1, (d) K2, (e) K3 and (f) K4.

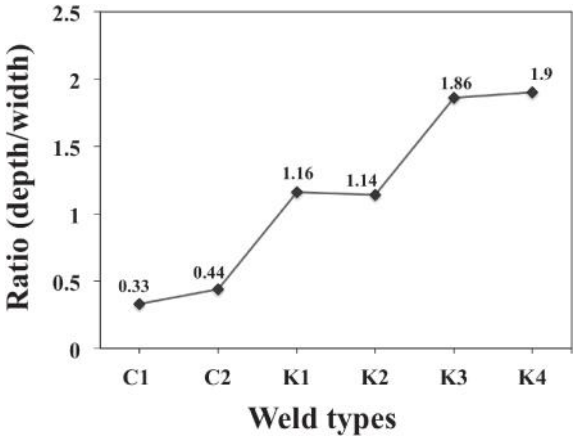

Fig. 4 Depth to width ratio of the welds.

Table 2 EDS elemental analysis of the weld seams.

Spectrum	Spectrum	Ti (at%)	Ni (at%)	O (at%)
C1	1	49.06	50.94	0
	2	47.98	52.02	0
	3	48.35	51.65	0
	4 (matrix)	49.33	50.67	0
C2	1	52.57	41.46	5.97
	2	28.34	27.24	44.43
	3(matrix)	46.29	53.71	0
K1	1	48.22	51.78	0
	2	48.66	51.34	0
	3	50.67	30.21	19.12
	4 (matrix)	49.62	50.38	0
K2	1	46.58	51.64	1.77
	2	48.92	51.01	0.06
	3	53.56	35.37	11.07
	4 (matrix)	49.13	50.87	0
K3	1	49.22	50.78	0
	2	41.11	44.59	14.30
	3	48.68	51.32	0
	4 (matrix)	48.47	51.53	0
K4	1	48.06	51.93	0.01
	2	30.72	31.81	37.47
	3	42.15	45.44	12.65
	4 (matrix)	48.93	51.07	0

welding speed, the amount of intermixed melt zone produced is small due to lower input energy, hence a narrow width and lower weld penetration are formed.[19] Different weld shapes were observed under keyhole-welding conditions. Weld seams of medium-welding parameters showed wine-cup shape weld seams with the presence of porosity in the weld-fusion zone. K1 with lower laser power was prone to form porosity more than K2. In contrast, K4 keyhole weld with high values in laser power and welding speed showed narrow weld seam without porosity. Depth to width ratio of the welds is also an important factor to evaluate the weld quality. C1 showed the worst depth to width ratio while K2 exhibited the maximum value of the ratio (Fig. 4).

3.2 Microstructure investigations

Figure 5 and Table 2 show microstructure observations of the welds using FESEM and EDS elemental analysis. The conduction weld of C1 showed a different microstructure compared with the other weld seams. It comprised a net-shaped microstructure inside the grains with an average diameter of 1.5 μm. Moreover, no precipitates and oxides were observed in the fusion zone of C1. In contrast, the conduction weld of C2 presented the largest oxide particles among all the welds. Keyhole-type weld seams of K1 and K2 included similar particles and microstructure. Similarly, K3 and K4 were also the same in microstructure. Figure 6 illustrates carbon contents of base metal and weld seams. It is clear that the heat-conduction-type weld of C1 included the highest carbon content and keyhole-type welds have lower amounts, which may be related to the preferential volatilization of carbon at a high power density of keyhole welding. Interestingly, keyhole-type welds contained lower carbon than base metal, whereas conduction-type welds presented higher carbon values than the base metal.

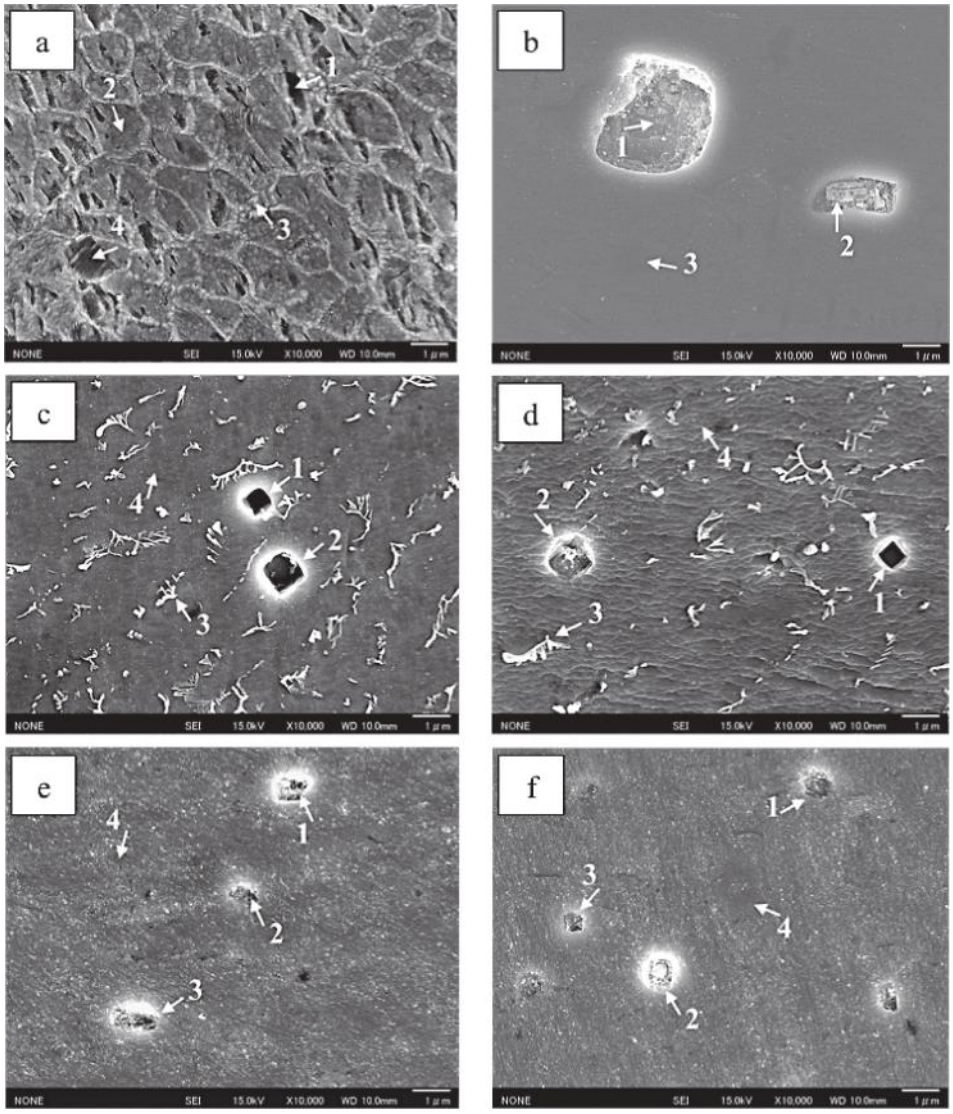

Fig. 5 Microstructure of the fusion zones: (a) C1, (b) C2, (c) K1, (d) K2, (e) K3 and (f) K4.

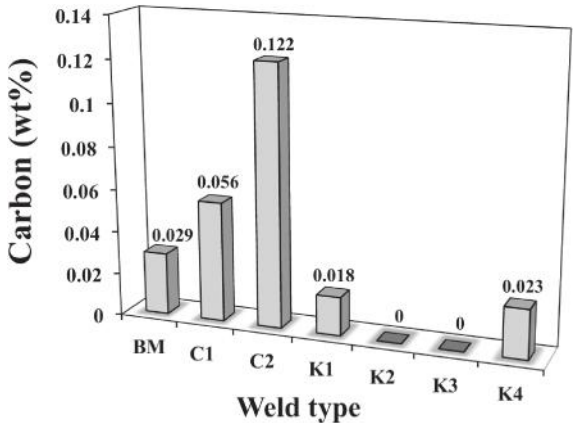

Fig. 6 Carbon content of weld seams.

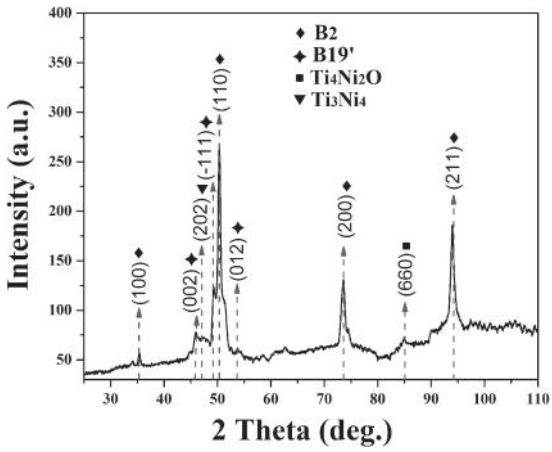

Fig. 7 XRD peak pattern of base metal.

XRD patterns of the base metal and weld seams are presented in Fig. 7 and Fig. 8. Base metal included austenite (B_2), martensite (B19′) at room temperature along with Ti_4N_2O and Ti_3Ni_4. Type C1 included austenite (B_2), martensite (B19′) and Ti_3Ni_4 but the peak intensity of the (200) plane was very small. Moreover, (110) along with (200) peaks associated with the austenite phase were not detected in C2. According to Hsu *et al.*,[20] this abnormal intensity in the laser welds of Ti–Ni results from texture evolution during solidification of the fusion zone. Martensite (B19′) and precipitates were not observed in C2. Keyhole-laser welds of K1, K3 and K4 showed austenite peak patterns

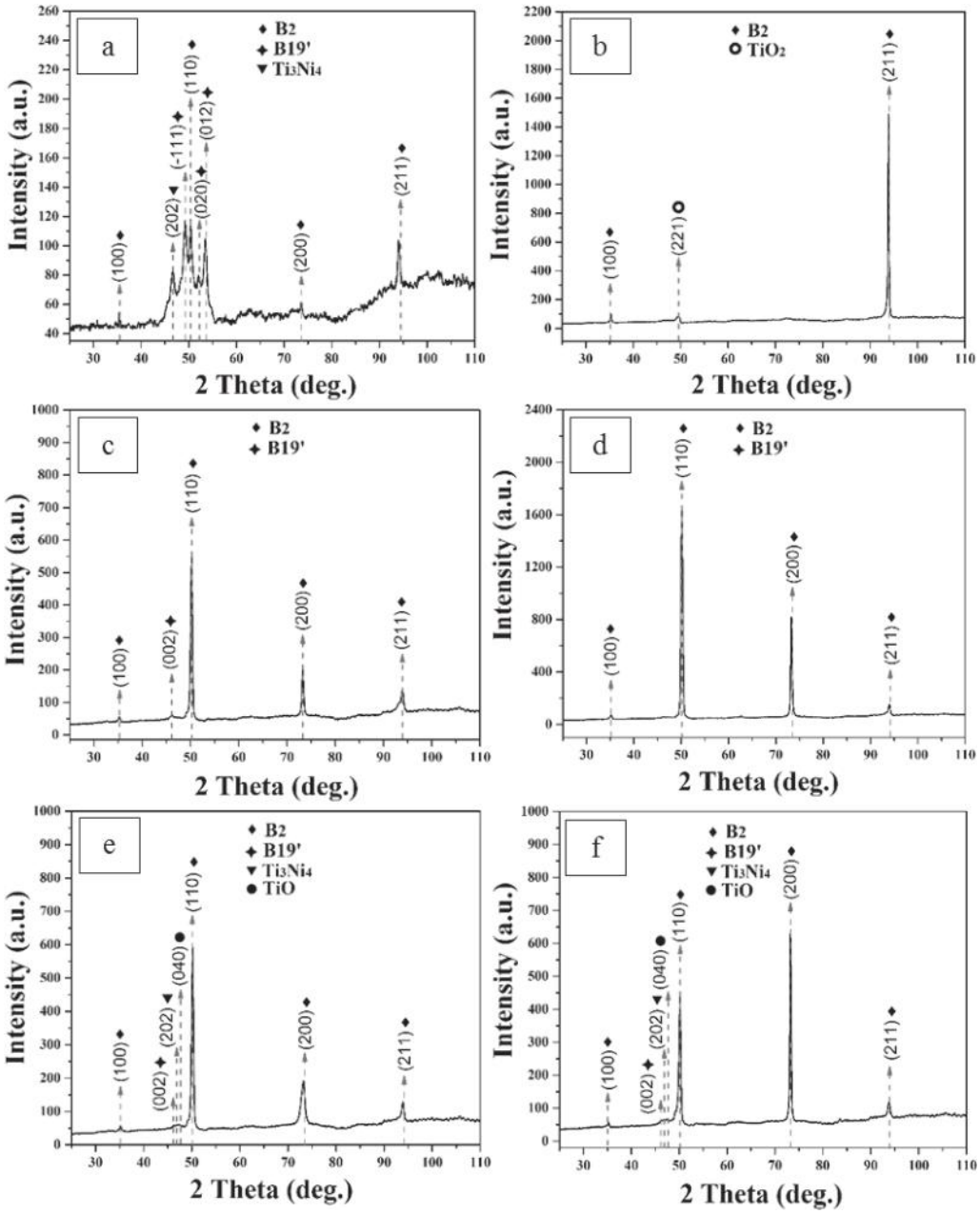

Fig. 8 XRD peak pattern of welded seams: (a) C1, (b) C2, (c) K1, (d) K2, (e) K3 and (f) K4.

as a dominant phase, along with a small amount of martensite but this phase was not observed in K2. Only small amount of Ti_3Ni_4 precipitates were observed in the K3 and K4 keyhole-weld seams, which indicates that these precipitates have dissolved during laser welding and according to Yan *et al.*,[21] heat treatment is helpful to obtain them again. It is important to note that in Ti–Ni welds, minimal martensite fraction is preferred owing to the undesirable effect on superelastic properties.[22] Because the superelastic effect is dependent on the amount of austenite available to undergo the stress-induced transformation, the presence of martensite at room temperature will have an implication on the functional behaviour of the welded joints. The martensite phase formation is related to the energy introduced to the welds. As shown in Table 1, heat input of keyhole welds is 5 to 10 times lower than for conduction welds.

Figure 9 shows EBSD analysis of the base metal. Figure 10 and Fig. 11 correspond to the C1 and K2 as heat-conduction-type and keyhole-type welds, respectively. EBSD test specimens were cut from the centre of the fusion zones. The texture was studied in both normal and transverse directions. Average grain size of the base metal was about 15 μm, but grains coarsened with different morphology to the average size of 30 μm in C1 and 81 μm in K2 weld seams. As shown in Fig. 9 in the base metal, a random texture was detected in the normal direction but grains oriented slightly to ⟨100⟩ in the transverse observation. This trend was stronger in the weld seams with higher texture intensities of 5.169 and 4.34, as shown in Figs. 10 and 11.

This phenomenon can be explained by the mechanism of competitive grain growth during weld-pool solidification, which is known as easy growth direction. ⟨100⟩ is the easy growth direction in the cubic structure metals.[23]

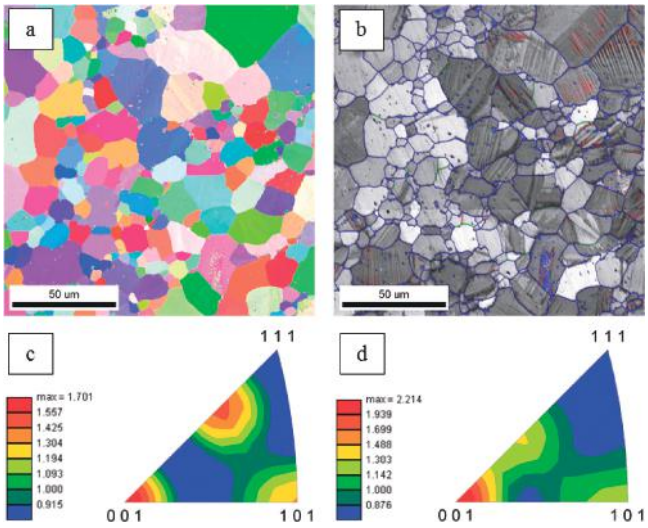

Fig. 9 EBSD of base metal: (a) inverse pole figure, (b) image quality map, (c) texture along the normal direction (ND) and (d) texture along the transverse direction (TD).

3.3 Phase transformation

Figure 12 shows phase transformation thermograms of the base metal and weld seams. The base metal showed $B19' \rightarrow B_2$ during heating and $B_2 \rightarrow R$ and $R \rightarrow B19'$ during cooling. The weld seams exhibited a similar phase transformation during heating but the single transformation of $B_2 \rightarrow B19'$ occurred in the cooling process compared with the base metal curve. The peak intensity of the DSC curve associated with C1 was the most similar to the base metal, although temperatures of the phase transformations moved to higher temperatures. It is known that increase in Ni content leads to local composition variation and decline of the martensite start temperature (Ms). Figure 13 shows that the Ms corresponds to the base metal and welded seams. Oliveira *et al.*[24] explained that the increase in transformation temperature is due to Ni-rich Ti_3Ni_4 in the heat-affect zone and Ni volatilization in the fusion zone. However, in our study, as shown in the XRD patterns, precipitates of Ti_3Ni_4 were detected in the C1 conduction weld as well, which can cause an increase in the transformation temperatures. By

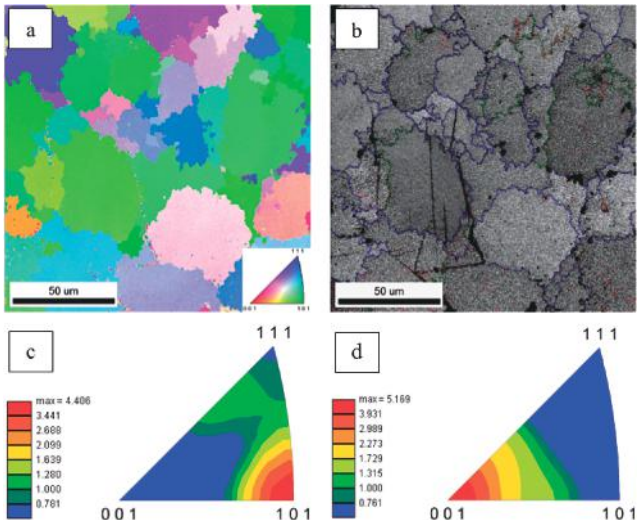

Fig. 10 EBSD of C1: (a) inverse pole figure, (b) image quality map, (c) texture along the normal direction (ND) and (d) texture along the transverse direction (TD).

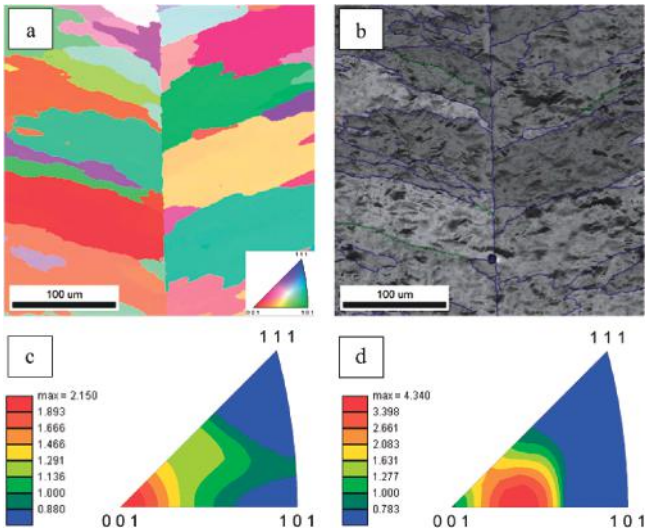

Fig. 11 EBSD of K2: (a) inverse pole figure, (b) image quality map, (c) texture along the normal direction (ND) and (d) texture along the transverse direction (TD).

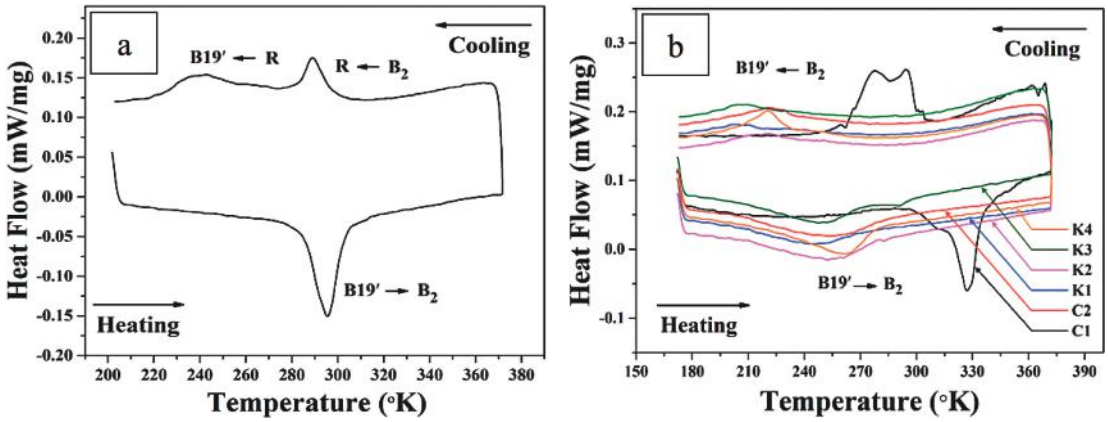

Fig. 12 DSC thermographs of (a) base metal and (b) weld seams.

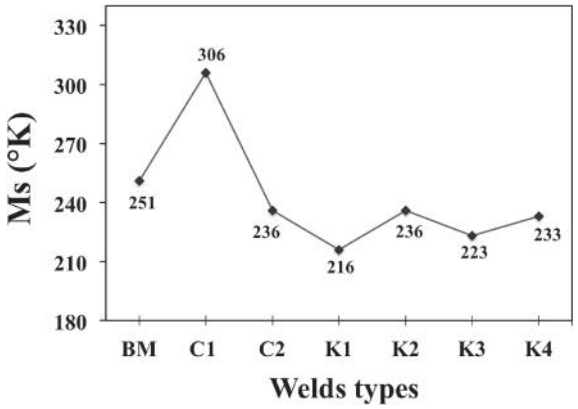

Fig. 13 Martensite start temperature (Ms) of the base metal and welded seams.

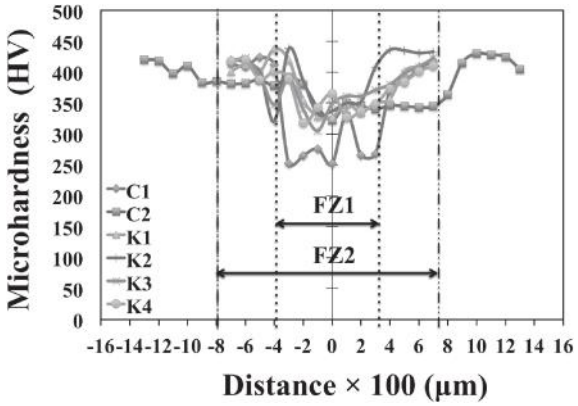

Fig. 14 Linear microhardness profile of weld seams; FZ2: fusion zone of C2 and FZ1: fusion zone of other welds.

contrast, corresponding transformation peaks of other weld seams moved to lower temperatures due to the absence of Ti_3Ni_4 in the weld zone. On the other hand, Chan *et al.*[25] suggested that three main reasons contribute to reducing the transformation temperatures in the laser welds, which conform to the DSC results of the current study; (a) compositional variation and precipitation formation in the weld pool, which leads to change in the Ni/Ti ratio, (b) coarse grain evolution in the fusion zone, which reduces nucleation sites of the martensite phase and (c) increasing the residual stress in the weld. Coarse grains and precipitations induce lattice distortion in the weld, which causes residual stress. Residual stress inhibits the martensitic transformation by hindering the reorientation process.

3.4 Microhardness analysis

Figure 14 shows linear microhardness test results, including base metal, heat-affected zone and fusion zone from both sides of the welds. There is a decline in the microhardness values of the fusion zones compared with the base metal but this reduction is considerable in C1. It is believed that the Hall–Petch relation by the following equation can be useful in explaining the hardness behaviour dependence on grain diameter in polycrystalline alloys.[26,27]

$$H = H_0 + kd^{-1/2}, \quad (2)$$

where H is the hardness of a polycrystalline metal, d is the grain diameter and H_0 and k are constants. As discussed in the EBSD analysis, grains grew radically after welding and, therefore, hardness reduced. Moreover, based on EDS elemental analysis, all welds included oxide particles, whereas no oxide was detected in C1, which supports the results of lower hardness.

4. Conclusions

In this research work, heat-conduction-type and keyhole-type laser welding systems under different laser power and welding speed were used to study the welding parameters that are suitable for joining Ti–51 at%Ni SMAs produced by SPS. In summary, the following conclusions can be drawn.

(1) Cross section of the welds revealed that depth to width ratio of the welds increased by increasing laser power and welding speed (keyhole type), even though at high laser powers, weld seams suffered from humping. Therefore, medium laser power and travel speeds (3 kW and 1.5 to 2 m/min) are suitable conditions for disc laser welding of Ti–51 at%Ni SMAs.

(2) Equiaxial grains formed in the centre of the heat-conduction-type weld but keyhole-type welds showed columnar growth of the grains towards the weld centreline and their preferential orientation to the ⟨100⟩ direction in EBSD results was observed.

(3) XRD peak pattern of the conduction weld was similar to the base metal, austenite and martensite mixture with more martensite evolution. The martensite phase declined in the keyhole-type welds and it was not detected in K2. Abnormal peak intensities were detected for (211) in the conduction weld of C2 and (200) in the keyhole weld of K4.

(4) DSC investigations showed that phase transformation peaks of the heat-conduction-type weld were similar to the base metal while corresponding peaks of the phase transformation in other weld seams were small and shifted towards lower temperatures. This can be explained by deviation in the Ni/Ti ratio via precipitations formation, reduction of martensite nucleation sites and increasing the residual stress due to grain coarsening after welding.

Acknowledgement

The authors would like to thank the Ministry of Higher Education of Malaysia for the Malaysian International Scholarship and research funding under FRGS Vote No R.J13000.7824.4F810 as well as Universiti Teknologi Malaysia and Joining & Welding Research Institute (JWRI) Osaka University Japan for providing the research facilities.

REFERENCES

1) T. Maeshima and M. Nishida: Mater. Trans. **45** (2004) 1096–1100.
2) A. Ikai, K. Kimura and H. Tobushi: J. Intell. Mater. Syst. Struct. **7** (1996) 646–655.
3) J.P. Oliveira, D. Barbosa, F.M.B. Fernandes and R.M. Miranda: Smart Mater. Struct. **25** (2016) 03LT01.

4) X. Zhao, L. Lan, H. Sun, J. Huang and H. Zhang: Mater. Lett. **64** (2010) 628–631.
5) S. Katayama: *Handbook of laser welding technologies*, (Woodhead Publishing, Cambridge, 2013) pp. 142–143.
6) C.W. Chan and H.C. Man: Opt. Lasers Eng. **49** (2011) 121–126.
7) A. Falvo, F.M. Furgiuele and C. Maletta: Mater. Sci. Eng. A **481–482** (2008) 647–650.
8) G.R. Mirshekari, A. Saatchi, A. Kermanpur and S.K. Sadrnezhaad: Opt. Laser Technol. **54** (2013) 151–158.
9) J. Vannod, M. Bornert, J.E. Bidaux, L. Bataillard, A. Karimi, J.M. Drezet, M. Rappaz and A. Hessler-Wyser: Acta Mater. **59** (2011) 6538–6546.
10) J.P. Oliveira, F.M. Braz Fernandes, R.M. Miranda, N. Schell and J.L. Ocana: Mater. Charact. **119** (2016) 148–151.
11) L. Krone, E. Schüller, M. Bram, O. Hamed, H.P. Buchkremer and D. Stöver: Mater. Sci. Eng. A **378** (2004) 185–190.
12) C. Shearwood, Y.Q. Fu, L. Yu and K.A. Khor: Scr. Mater. **52** (2005) 455–460.
13) L. Zhang, Y.Q. Zhang, Y.H. Jiang and R. Zhou: J. Alloys Compd. **644** (2015) 513–522.
14) E.O. Correa, S.C. Costa and J.N. Santos: J. Mater. Process. Technol. **209** (2009) 3937–3942.
15) A. Kurt, H. Ates, A. Durgutlu and K. Karacif: Weld. J. (Miami, Fla) **83** (2004) 34–37.
16) A. Unt and A. Salminen: J. Laser Appl. **27** (2015) S29002.
17) M. Takanori, N. Nozomi, U. Junko and K. Katsuyoshi: Trans. JWRI **40** (2011) 63–68.
18) T. Wang, J. Chen, X. Gao and W. Li: Appl. Sci. **7** (2017) 299.
19) W. Wang, X. Yang, H. Li, F. Cong and Y. Liu: Chinese J. Lasers **35** (2008) 291–296.
20) Y.T. Hsu, Y.R. Wang, S.K. Wu and C. Chen: Metall. Mater. Trans., A **32** (2001) 569–576.
21) X. Yan and Y. Ge: J. Mater. Eng. Perform. **23** (2014) 3474–3479.
22) J.P. Oliveira, R.M. Miranda, N. Schell and F.M.B. Fernandes: Int. J. Fatigue **83** (2016) 195–200.
23) D. Yang, H.C. Jiang, M.J. Zhao and L.J. Rong: Mater. Des. **57** (2014) 21–25.
24) J.P. Oliveira, F.M. Braz Fernandes, R.M. Miranda and N. Schell: Shape Mem. Superelasticity **2** (2016) 114–120.
25) C.W. Chan, H.C. Man and T.M. Yue: Metall. Mater. Trans., A **42** (2011) 2264–2270.
26) E.O. Hall: Nature **173** (1954) 948–949.
27) N.J. Petch: J. Iron Steel Inst. **173** (1953) 8–25.